Test Beam Analysis and Commissioning of a New Beam Telescope for DRD1

Mirac Noyan Oezdemir

A report submitted as part of the CERN Summer Student Programme
Conseil Européen pour la Recherche Nucléaire
European Council for Nuclear Research
Geneva, Switzerland

September 2025

First Supervisor M.Sc. Karl Jonathan Floethner
Second Supervisor Dr. Eraldo Oliveri

Contents

1 Introduction

This report presents the commissioning of a new Micromegas-based beam telescope for the DRD1 collaboration and the analysis of data collected during the SPS summer test beam campaign. The work included characterization of the gaseous detectors, assembly and operation of the telescope, and evaluation of its performance under beam conditions.

Gaseous detectors are widely used in particle physics for tracking charged particles. Ionization by traversing particles produces electrons that drift and amplify, generating measurable signals. Their large active area, low material budget, and good spatial resolution make them suitable for precise tracking over extended regions.

Micromegas (MICRO-MEsh GAseous Structure) detectors, invented in 1996 [9], consist of a thin micromesh separating the drift region from a narrow amplification gap. Electrons produced in the drift region pass through the mesh and undergo avalanche multiplication in the amplification region, producing high-gain signals.

The GDD laboratory and DRD1 collaboration benefit from complementing the existing GEM telescope with this newly commissioned Micromegas system. Fabricated using the novel thermal bonding technique, the telescope provides a larger sensitive area (15 cm × 15 cm) than the GEM telescope (10 cm × 10 cm) and enables tracking over a wider flux. The setup also allows integration of more devices under test (DUTs). The readout electronics, acquired through AIDAinnova funding, provides modern front-end readout for common test beam infrastructure.

A schematic view of a Micromegas cross-section is shown in Fig. 1.

1.1 Tracking detectors

The new telescope for the DRD1 collaboration consists of three so-called thermal bonded Micromegas (TBM), with a fourth spare, referring to their manufacturing technique [7]. The Micromegas have IDs that are numbered from two to five. The standard method for producing Micromegas detectors is the "bulk" process, which relies on photoetching [8, 16]. However, this approach requires advanced instrumentation and processing, which limits the accessibility of Micromegas production.

To overcome these limitations, the thermal bonding technique was developed as an alternative. Its main advantages include a simplified manufacturing procedure and the elimination of chemical agents [7]. The procedure of thermally bonding the mesh on the PCB is illustrated in Fig. 2. A more detailed description and illustration of the thermal bonding technique is shown in [7].

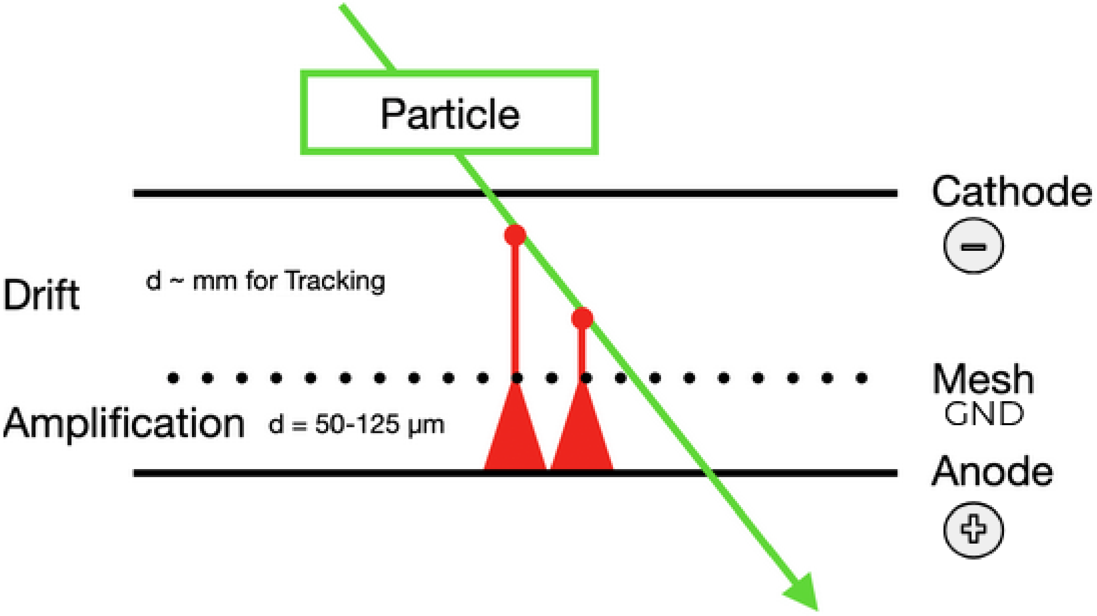

Figure 1: Schematic overview of a Micromegas detector. A charged particle traversing the drift gap produces electron–ion pairs along its track. The electrons drift towards the amplification region following the electric field lines, where they undergo multiplication due to the strong electric field. Image adapted from [3].

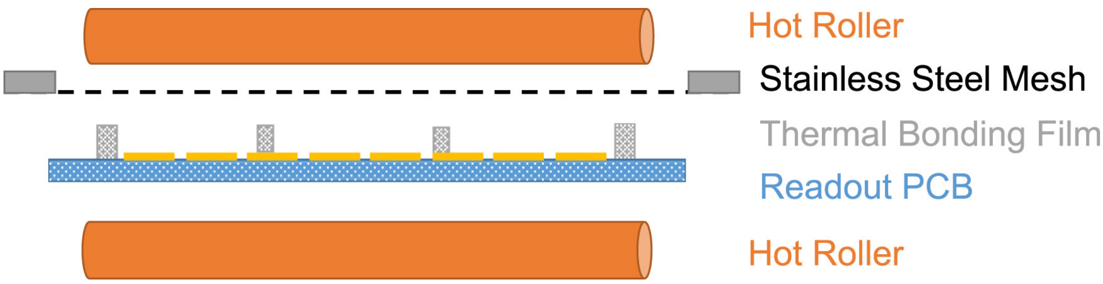

Figure 2: The image shows the procedure of the thermal bonding method. Images adapted from [7].

The thermal bonded Micromegas used for the telescope were provided to the GDD laboratory for this summer student project by DRD1 collaboration members from USTC and were manufactured jointly by USTC and the JIANWEI company. The detectors feature a drift gap of 5 mm and an amplification gap of 100 µm. Readout is performed using x- and y-strips with a pitch of 400 µm and 384 channels per axis, resulting in a sensitive area of 150 mm × 150 mm. The supporting pillars that hold the mesh have a diameter of 1 mm and are arranged in a hexagonal pattern with a pitch of 10 mm. The mesh itself is made of stainless steel, with an opening rate of 51% and a density of 325 LPI. The mesh opening rate of a Micromegas refers to the fraction of open area (optical transparency) of the woven stainless steel mesh. A schematic structure of the prototype is shown in Fig. 3.

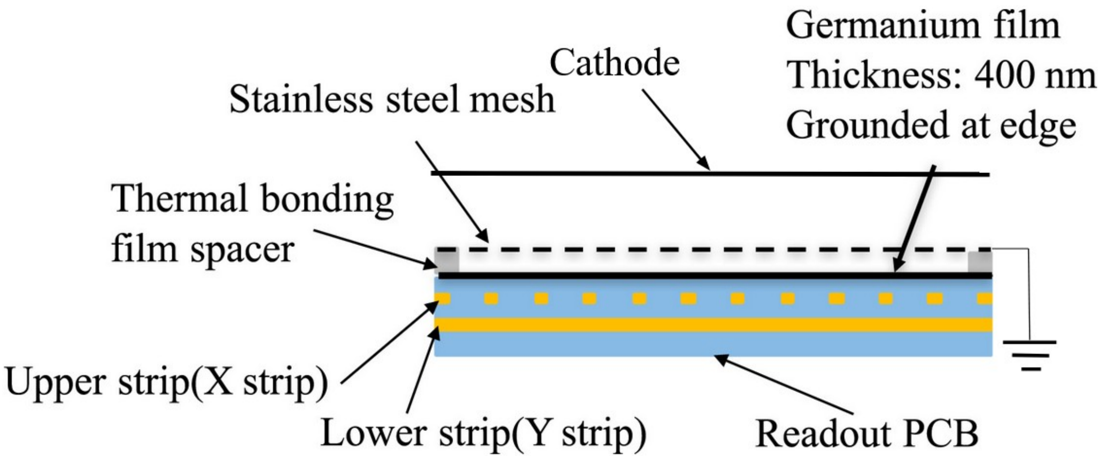

Figure 3: Schematic representation of the Micromegas prototype at the anode with a 2D strip readout. The ground can be connected to the anode or mesh. Image taken from [7].

One distinctive feature of the Micromegas used in the telescope is the resistive layer on the anode. This layer enhances the high-voltage (HV) stability of the detector and protects the readout electronics by limiting the charge flow to the readout strips, which is particularly important in the event of sparks. Sparks, also referred to as discharges, are sudden, localized breakdowns of the gas caused by excessively high electric fields. They occur when the electron avalanche in the amplification region becomes sufficiently large to trigger a self-sustaining ionization, analogous to a miniature lightning strike inside the detector.

The effect of the resistive layer on the HV stability of the Micromegas detector is illustrated in [11].

2 Laboratory measurements

This section provides a detailed description of the experimental setup used in the GDD lab for the detector characterizations and the results of the characterization.

2.1 GDD laboratory setup

The GDD laboratory setup was used to characterize the detector properties, such as gain and drift scans, as well as understanding the effect of collimation on the energy resolution. A detailed explanation of these scan types is provided in the following section. A photograph of the setup is shown in Fig. 4. The laboratory setup consists of the following components:

- Square detector mounted on the green PCB
- Red high-voltage (HV) cables connected to the HV supply to vary the anode, mesh, and cathode voltages
- Cooling fan
- Gas connections with the blue cable facing the screen and the white cable facing inward, both connected to the Micromegas metal frame
- Six black VMM3a hybrids
- Power box for the hybrids with orange and black power cables
- Radioactive ^{55}Fe source (on the left) with metal source holder placed on the detector corner
- Multimeter
- APIC preamplifier, amplifier, and shaper (yellow box)
- Oscilloscope

Two types of readouts are possible. The first is via the mesh or strips using the APIC, which is discussed in this subsection; a corresponding circuit diagram is shown in Fig. 5. The second type is the strip readout using the VMM3a/SRS (Scalable-Readout-System), which is described in the following subsection.

The mesh signal readout, shown as the red circuit in Fig. 5, operates as follows. The induced signal is forwarded through the safe high-voltage (SHV) cable connected to the mesh, and is then split over a resistor and capacitor in parallel. This network acts as a filter to suppress low-frequency noise. In this readout circuit, the strips are terminated with $50\,\Omega$. The high-frequency component of the mesh signal passes through the capacitor and is fed into the APIC, and subsequently into the MCA. To achieve improved energy resolution, one can collimate the irradiated area of the detector with the radioactive source, enabling uniformity studies.

The strip readout, represented by the blue circuit in Fig. 5, works differently. Here, the mesh is terminated with $520\,\mathrm{k\Omega}$, while the strip signals are capacitively coupled and combined into a single cable. The same filtering scheme with a resistor and capacitor is applied, ensuring that only the high-frequency component is forwarded. This filtered signal is then processed by the APIC and finally digitized by the MCA.

The gas flow was first around $2\,\mathrm{L\,h^{-1}}$, but was afterwards increased to $5\,\mathrm{L\,h^{-1}}$, because a higher gas flow reduced the impact of humidity accumulation in the detector. This

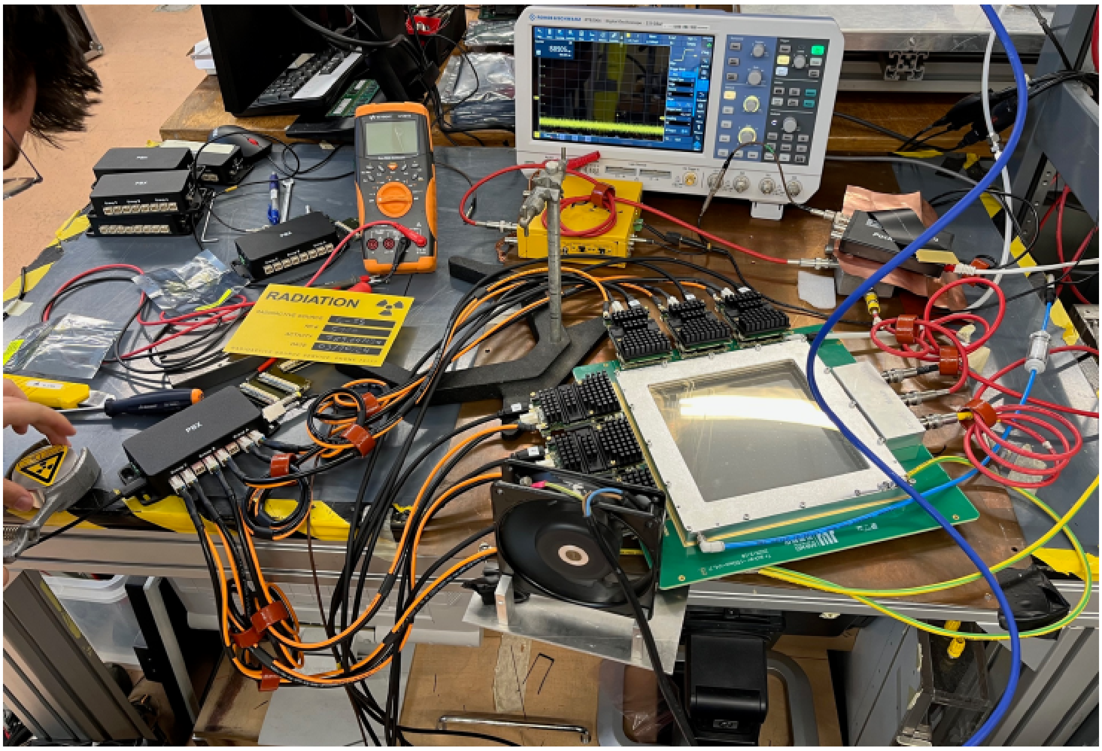

Figure 4: Setup in the GDD lab. The picture shows the Micromegas detector with its gas and HV supply cables and the electronics for the mesh and strip VMM3a/SRS readout. A fan was used for cooling the VMM3a readout setup and an oscilloscope for visualizing the waveforms.

is critical for the avalanche stability of the detectors and reduces the frequency of discharges.

2.2 Gain scan

The ^{55}Fe source is commonly used for energy calibration in gaseous detectors, as it provides well-defined X-rays at 5.9 keV. When these photons interact with the detector gas, primarily through the photoelectric effect, electrons are ejected and initiate the ionization process. Depending on whether the characteristic argon photon produced during the relaxation process is fully absorbed or escapes, either the full photopeak or escape peaks at lower energies are observed. An example of such a spectrum is shown in Fig. 6. Additionally, electronic noise dominates the low-energy channels, producing an exponentially falling background.

A gain scan is then performed for Micromegas detectors to characterize their amplification behavior and determine the optimal operating voltage. By systematically varying the anode voltage and measuring the detector response, one can study how the gas gain evolves and identify the region where the detector provides sufficient amplification

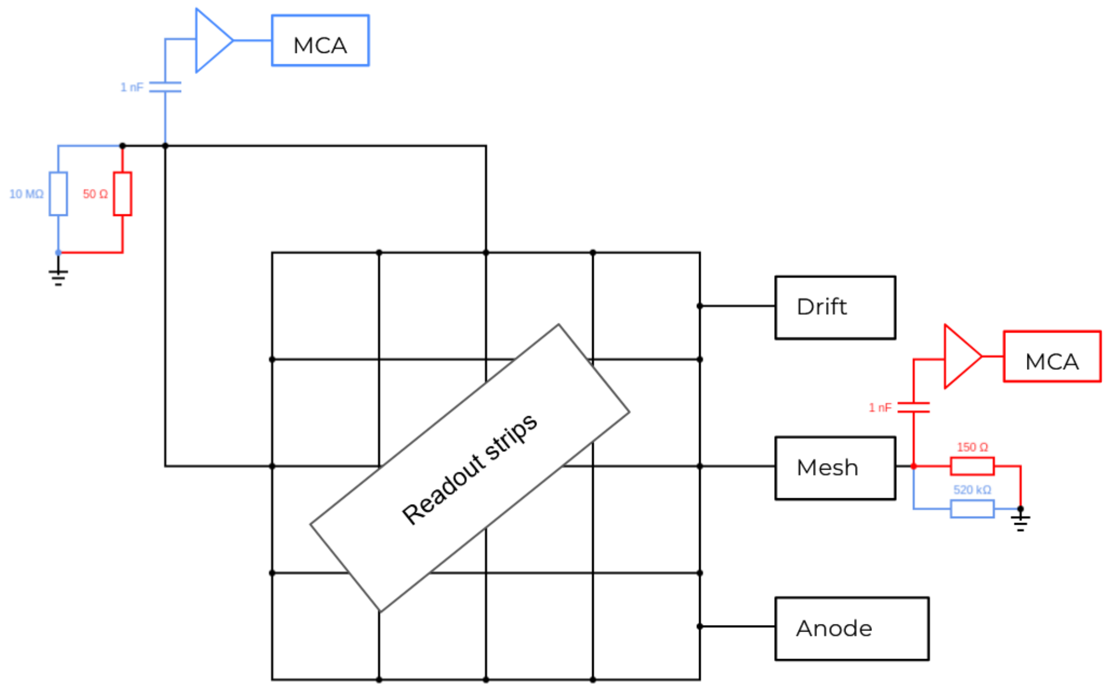

Figure 5: Schematic illustration of two readout circuits: (red) mesh readout with terminated strips, and (blue) strip readout with terminated mesh. Both circuits use a resistor–capacitor filter before the signal is sent to the APIC and MCA. The HV is connected to the anode, mesh, and cathode as shown in Fig. 3.

while maintaining stability and avoiding discharges. This procedure ensures that the Micromegas operates with a good signal-to-noise ratio, reliable efficiency, and minimal risk of damaging sparks. This scan used the previously shown red circuit.

Because the detector might exhibit a certain leakage current, the current difference between measurements taken with and without the source is used to estimate the output signal, as expressed in Eq. 1. The input current is calculated from the number of primary electrons (N_{prim}), the elementary charge e, and the full rate R_{full}. The latter is determined by recording MCA spectra with and without the ^{55}Fe source, calculating the rate difference, and plotting it as a function of the anode voltage. As shown in Fig. 6, the rate reaches a plateau of approximately 5000 Hz at around 630 V. This plateau is taken as the full rate R_{full}, which is then used in the gain calculation.

In the typical operation region of gaseous detectors, the gain exhibits an exponential dependence on the applied anode voltage. Therefore, exponential fits were applied to the gain data points for both Ar/CO_2 mixtures of 70/30 and 93/7. The results are presented in Fig. 7, where the left plot corresponds to MM4 with a 70/30 mixture and the right plot to MM3 with a 93/7 mixture. The uncertainties on the 93/7 mixture data points were estimated to be 15%, based on the average relative uncertainties observed for the 70/30 mixture. Both fits yield reasonable χ^2/NDF and p-values.

The gain scan for the Ar/CO_2 93/7 mixture is shown in Fig. 8. At low and intermediate voltages, the gain follows the expected exponential increase characteristic of avalanche multiplication. However, above gains of approximately 2×10^4, clear deviations from this exponential trend are observed. These deviations can be attributed to photon feedback: UV photons emitted during the avalanche may ionize or excite gas molecules elsewhere in the detector volume, producing photoelectrons that trigger secondary avalanches. This process leads to an artificial enhancement of the measured gain and indicates the onset of instabilities at very high amplification.

$$\text{Gain } G = \frac{I_{out}}{I_{in}} = \frac{I_{source} - I_{nosource}}{N_{prim} \cdot e \cdot R_{full}} = G_0 \cdot e^{\alpha \cdot U} \quad (1)$$

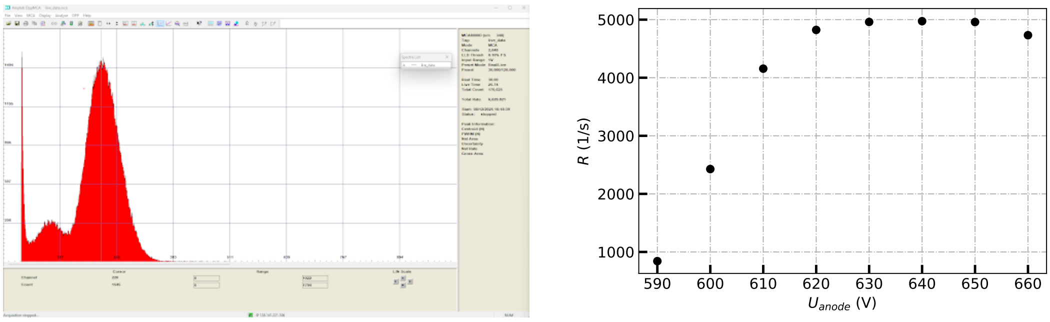

Figure 6: (Left) ^{55}Fe energy spectrum measured with the lab setup using the Amptek Pocket MCA. The ^{55}Fe source emits 5.9 keV photons that interact via the photoelectric effect, producing electrons which serve as ionizing particles. Escape peaks appear around 3.0 keV when argon fluorescence photons leave the detector volume, while the low-channel region shows an exponentially decreasing noise contribution. (Right) Rate scan of MM4 operated with an Ar/CO_2 (70/30) mixture. A plateau at 5000 Hz is reached at approximately 630 V, which is taken as R_{full} for the gain scan.

2.3 Drift scan

A drift scan is carried out for Micromegas detectors to study how the electron drift properties depend on the applied drift field. By varying the drift voltage, one can measure changes in electron transparency through the mesh, drift velocity, and overall signal formation. This allows identification of the optimal drift field that maximizes electron collection efficiency while minimizing losses due to recombination, attachment, or mesh intransparency. This measurements were taken using the blue circuit. The signal amplitudes were lower than for the red circuit, as the strips are capacitively

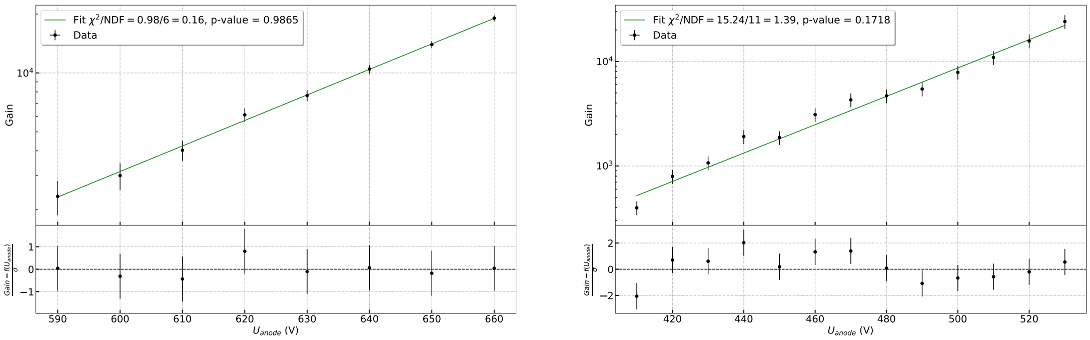

Figure 7: Exponential fits to the calculated gain data-points for Ar/CO_2 mixtures of 70/30 for MM4 (left) and 93/7 for MM3 (right). The uncertainties on the 93/7 mixture were estimated based on the 70/30 mixture fit to be 15%. Both fits have a good $\frac{\chi^2}{NDF}$ and p-values. The fit on the 93/7 data was made with a subset of data-points, as one leaves the proportional region, when increasing the voltage above 530 V.

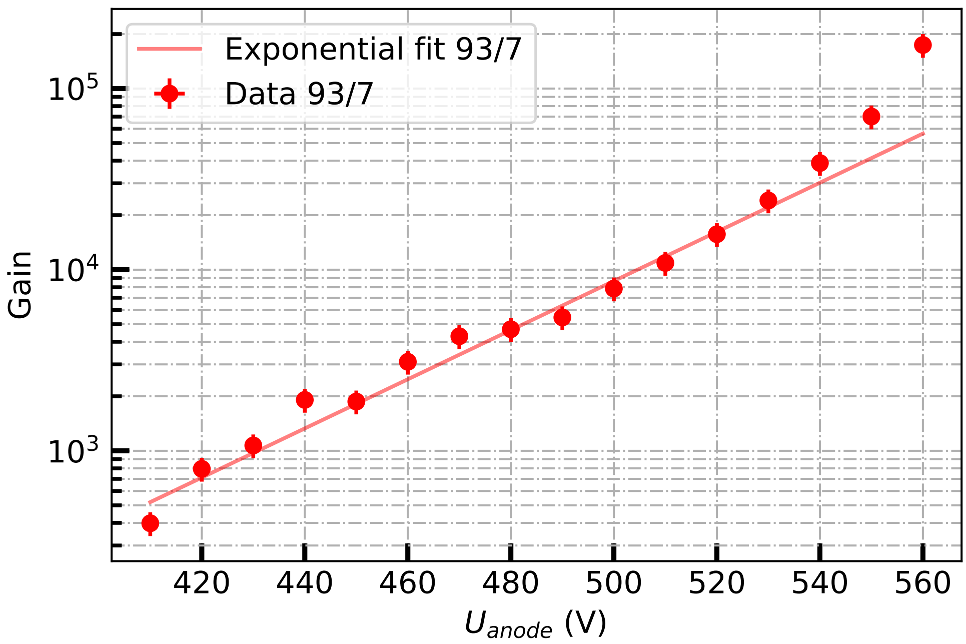

Figure 8: Gain scans for Ar/CO_2 mixture of 93/7. Deviations from the exponential behavior become visible above a gain of 2×10^4. These deviations can originate from photon feedback causing additional avalanches. This occurs when gas atoms are excited by the avalanche, emit UV photons, and subsequently create photoelectrons, which in turn initiate avalanches elsewhere in the detector.

coupled to each other, reducing the signal induction input for the APIC. This readout setup was chosen, to make a first step towards the strip VMM3a/SRS readout.

The experimental results of the drift scan are summarized in Fig. 9. The left panel shows the background-subtracted MCA spectra of MM3 for different drift voltages, where a distinct peak-shifting behavior is observed as the voltage is varied between 0 V and 1000 V. By fitting Gaussians to these spectra, the peak positions were extracted, revealing the trend shown in the right panel: an initial rise in channel number at low drift voltages, a plateau between 50 V and 300 V, followed by a linear decrease at higher voltages. The MCA spectra sometimes have a large increase in counts at low MCA channels, which could be attributed to a noise count fluctuations. This behavior can be understood from the evolution of the electric field lines, illustrated in Fig. 10. At low drift voltages, the mesh remains highly transparent, allowing most electrons to reach the amplification region. However, as the drift voltage is increased, an increasing fraction of the field lines terminate on the mesh instead of crossing it. Since drifting electrons follow these field lines, the transparency of the mesh is reduced, leading to a diminished number of electrons contributing to the signal. This would imply that at low drift voltages the mesh transparency is the highest. However, the data-point at 0 V does not have a comparable peak channel. This can be explained by the gas quality, as impurities like water vapor or oxygen impact the drifting of the electrons.

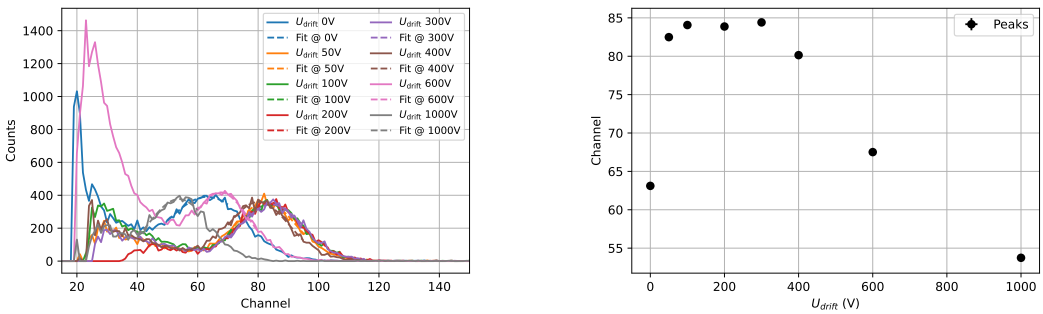

Figure 9: Results of the drift scan of MM3 are shown. The ^{55}Fe source was collimated to 1 mm. The left plot displays the background-subtracted MCA spectra for different cathode/drift voltages, with the anode voltage fixed at 510 V, and using an Ar/CO_2 (93/7) gas mixture. A clear peak-shifting behavior is observed when varying the drift voltage between 0 V-1000 V. This was quantified by fitting Gaussians to the peaks and extracting their x-positions. The corresponding peak channel numbers are presented in the right plot: they increase at low drift voltages, reach a plateau between 50 V and 300 V, and subsequently decrease linearly.

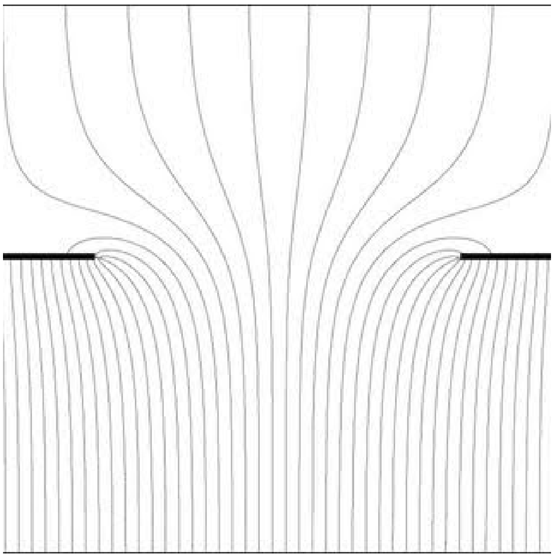

Figure 10: Electric field lines between the cathode, mesh, and anode are shown. The anode is located at the bottom of the image, and the cathode at the top. The black solid lines on the left and right represent parts of the mesh. Most field lines pass through the mesh; however, when the drift voltage is increased, more field lines terminate on the mesh. Since electrons follow the field lines while drifting, fewer primary electrons reach the amplification region. This effect is referred to as the reduction of the electron transparency of the mesh at higher drift voltages. Image taken from [4].

2.4 VMM3a/SRS readout

The second readout system implemented for the strip readout of the Micromegas detectors utilizes the VMM3a/SRS platform, which interfaces with the detector strips via Hirose connectors. The system is built around the VMM3a Application-Specific Integrated Circuit (ASIC), originally developed for the ATLAS New Small Wheel upgrade, which provides charge and time measurement capabilities. A feature of this system is the independent programmability of the electronic gain for each VMM3a chip. This programmability can be used for compensating for intrinsic detector response variations. The Scalable Readout System (SRS) supplies the supporting hardware and software infrastructure for VMM3a configuration, data acquisition management, and signal processing. A comprehensive description of the system's software, firmware, and hardware architecture is available in [10, 15, 1]. This readout chain was utilized for detector characterization, yielding the 2D hitmap and energy spectrum presented in Fig. 11, along with the gain uniformity and energy resolution analyses detailed in Fig. 12.

As evidenced by the ADC spectrum in Fig. 11, the x-strip signal exhibits a characteristic distribution comparable to the MCA spectrum obtained from mesh readout characterization in Fig. 6. In contrast, the y-strips demonstrate significantly reduced signal amplitude. This asymmetry originates from a manufacturing imperfection where the y-strips are embedded at a depth of $\mathcal{O}(100\,\mu\text{m})$ within the insulating layer, rather than $\mathcal{O}(10\,\mu\text{m})$. The increased distance to the anode plane substantially attenuates the induced signal, resulting in negligible initial signal detection on the y-strips. However, the electronic gain programmability of the VMM3a/SRS system permitted partial signal recovery through increased amplification, yielding the ADC distribution visible in

Fig. 11. The electronic gain in the lab setup for the x-strips was $3\,\mathrm{mV\,fC^{-1}}$, whereas the y-strips used an electronic gain of $12\,\mathrm{mV\,fC^{-1}}$ for the signal recovery.

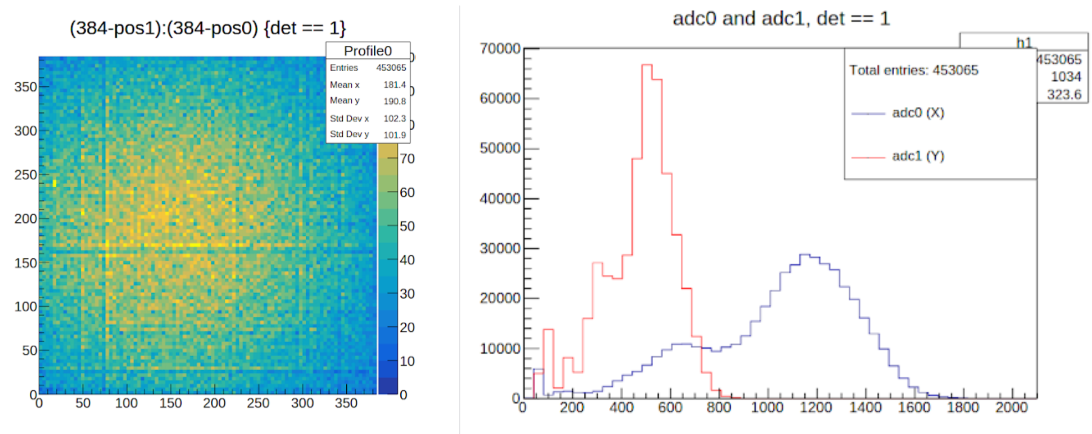

Figure 11: The left plot shows a 2D hitmap of the detector using the VMM3a/SRS strip readout. The right plot shows the ADC (or energy) distributions for the x- and y-strips. The signal on the x-strips looks like an ^{55}Fe spectrum, whereas the y-strips don't show the same behavior. This is due to a manufacturing error, where the y-strips are not $\mathcal{O}(10\,\mu\mathrm{m})$ deep in the insulating layer, but $\mathcal{O}(100\,\mu\mathrm{m})$. The signal is partially being recovered by increasing the electronic gain on the y-strips, as mentioned before. Both plots were generated for MM3.

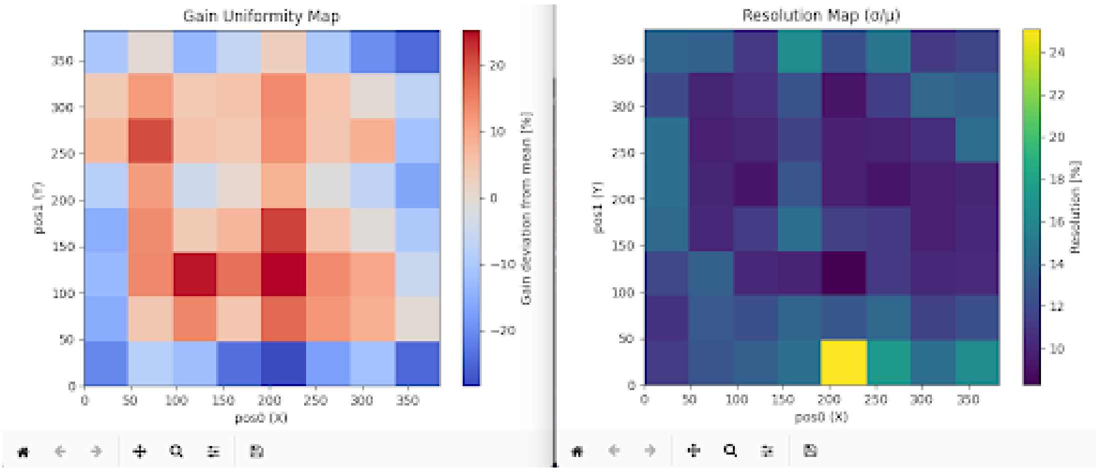

Figure 12: This figure shows the results of the uniformity study on MM3. The left plot splits the detector in 8x8 tiles and calculated the gain deviation from the mean detector gain in %. Deviations up to ±25% are visible. They occur due to minor manufacturing deviations or effects like mesh sagging. The right plot shows the relative energy resolution at one standard deviation after fitting a gaussian to the photopeak of the ADC distribution. The resolution varies from 8–18%, with one tile having a resolution of 24%.

The VMM3a software and firmware are currently under continuous development, with one recent addition being the implementation of an event counter [13]. This functionality allows synchronization with external setups and can be used as a trigger flag for the telescope. During the test beam campaign, the event counter was employed to acquire data triggered by the PICOSEC setup [5]. Aside from these externally triggered runs, the telescope data acquisition was generally operated in self-triggered mode.

Collimation of the radioactive source

Collimation improves the energy resolution of gas detectors by reducing detector ununiformities and minimizing the overlap of regions with different local gains. Without collimation, incoming radiation can interact across a wide area of the detector, where variations in electric field strength, amplification properties, or geometrical effects may exist. This leads to a mixing of signals originating from regions with slightly different effective gains, broadening the energy spectrum and worsening resolution. By restricting the incident particles to a narrower, well-defined region, collimation ensures that most interactions occur under similar detector conditions, thereby reducing these systematic variations and resulting in a sharper, more accurate energy peak.

This is shown in Fig. 13 and Fig. 14. This setup used the MM3 with an Ar/CO_2 mixture 93/7 and a gain of ≈ 20000. This subsection does not consider the ADC distribution of the y-coordinate, due to the previously mentioned effect. In Fig. 13 the energy resolution at FWHM is around 39% in the x-coordinate, due to the aforementioned effect, when the source is not collimated. However, when localizing the source to 3.6 cm, the energy resolution at FWHM improves to 25%.

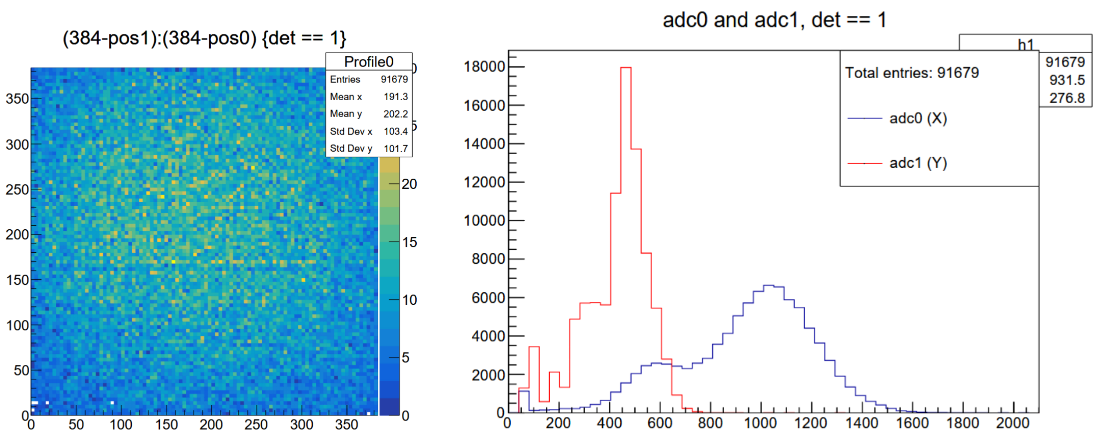

Figure 13: Uncollimated irradiation by the ^{55}Fe source. Left: 2D hitmap of strips. Right: ADC distributions for x- and y-coordinate. The ADC distribution for the x-coordinate has an energy resolution of $\approx 39\%$ at FWHM.

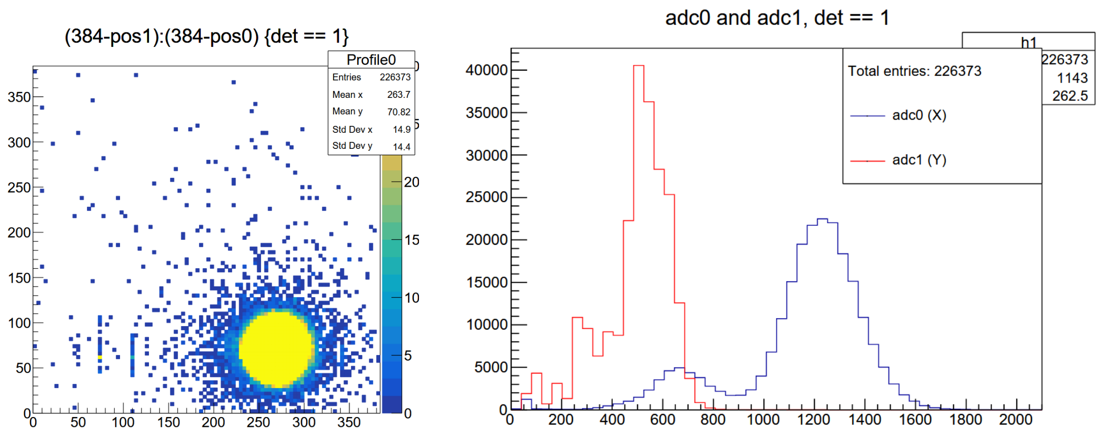

Figure 14: Collimated irradiation by the ^{55}Fe source. Left: 2D hitmap of strips, the irradiated area has a diameter of around 90 strips (≈ 3.6 cm). Right: ADC distributions for x- and y-coordinate. The ADC distribution for the x-coordinate has an energy resolution of $\approx 25\%$ at FWHM, improving significantly compared to the uncollimated irradiation in Fig. 13.

3 Test beam measurements and Corryvreckan analysis

This section presents the test beam setup and data together with a first look to the Corryvreckan results for track reconstruction.

3.1 North area test beam setup

The setup in the test beam area had a different purpose than the one in the laboratory. While the laboratory setup was primarily used to characterize and test the detectors, the telescope setup in the North Area was built for testing detectors or devices under test (DUTs). A picture of the Micromegas telescope is shown in Fig. 15. The DUTs can be mounted between the Micromegas, and the telescope can be extended from its original length of 70 cm up to 140 cm. The telescope consists of the following components:

- 3 thermal-bonded Micromegas
- 3 VMM3a hybrids with power supplies and HDMI cables
- 2 HV power supplies, one power supply for 2 detectors
- 2 SRS minicrates, each equipped with 2 dVMMs and 2 FECs
- 1 clock, for time synchronization
- 2 network switches (one for data transfer, the other for remote HV control)

- 5 cooling fans

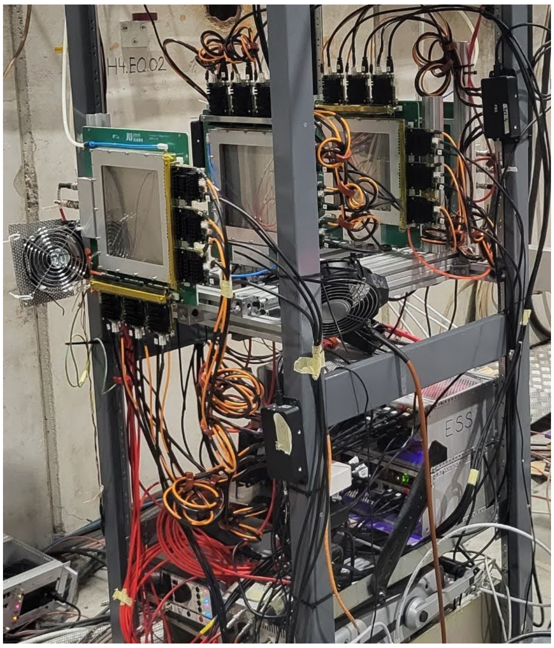

Figure 15: This picture shows the new Micromegas telescope for the DRD1 collaboration. In this setup, the signal is read out using the VMM3a/SRS system. The signal is transmitted from the VMM3a via HDMI cables to the back of the SRS minicrate (e.g. the metal crate labeled "ESS"). Inside the minicrate, the signal is digitized and pre-processed before being forwarded to a PC through a network cable.

As indicated in Fig. 15, the readout chain plays a central role in the operation of the telescope. The detector signals are first amplified and shaped by the VMM3a ASICs located on the hybrids. These signals are then transmitted via HDMI cables to the SRS minicrates, where they are digitized and pre-processed by the dVMMs and FECs. The processed data is subsequently transferred to a PC through standard network connections for storage and analysis. A detailed description of the VMM3a/SRS readout is given in [10].

3.2 Beam profiles & DUT HV scan

The results presented in this section were obtained with the test beam setup described in Sec. 3.1. To increase the available dynamic range, the electronic gain of the x-strips of each thermally bonded Micromegas was set to $6\,\mathrm{mV\,fC^{-1}}$, and a continuous gas flow of $5\,\mathrm{L\,h^{-1}}$ was maintained.

At the beginning of the measurement campaign, the Micromegas detectors in the telescope were rotated around their axes to mitigate possible systematic effects originating from manufacturing tolerances in the strip orientation. After initial data taking, however, it was observed that MM5 exhibited frequent discharges. To stabilize the system, all tracker x-coordinates were aligned, as now it was evident that there is a strong coordinate (x-coordinate), and MM5 was replaced with MM4. The latter had shown almost no signal induction during laboratory tests and was therefore brought to the Micro-Pattern Technologies (MPT) workshop for cleaning. After being cleaned it showed a comparable stability as MM3.

The comparatively better performance of MM3 in the laboratory may also be attributed to the fact that it was continuously connected to the gas line, ensuring a constant flushing of the detector volume. In contrast, the other Micromegas chambers, which were disconnected between measurements, could have accumulated a certain level of humidity.

For the test beam measurements, a ternary $Ar/CO_2/iC_4H_{10} = 93/5/2$ gas mixture was used. The addition of isobutane provides improved stabilization of the discharge behavior, and the same composition is employed in the ATLAS New Small Wheel. During operation, the detectors were run at a gas gain of approximately 80 000. The increased performance of MM2, which was also sporadically discharging, compared to the GDD lab could be attributed to a combination of the gas flushing together with the new gas mixture.

During the test beam campaign, several measurement series were conducted to characterize the performance of the DUT under different conditions. The DUT was a thin-mesh Micromegas [14]. Initial runs involved muon-induced HV scans of the DUT from 390 V to 500 V, with the tracker operated at a gain of approximately 25 000. Subsequently, pion HV scans were performed from 470 V to 500 V, during which MM5 was exchanged with MM4 and the tracker x-coordinates were aligned to improve stability and reduce discharges.

Following these preparatory measurements, multiple muon HV scans were carried out over overlapping voltage ranges (380 V–500 V) with increased tracker gain of roughly 80 000, incorporating the MM5 replacement and x-coordinate alignment. One series specifically used MM2 as the DUT, while the usual DUT was employed as part of the tracker. Additional measurements included scans with extended telescope arms to study detector performance over a larger distance. Finally, a dedicated run was performed with the DUT at 495 V, high tracker gain, extended telescope arms, and triggered operation using the MCP from the PICOSEC [5] setup to synchronize data acquisition.

A beam profile with its corresponding ADC distribution is shown in Fig. 16. The beam exhibits a diamond-like shape, with a slight shadow visible in the right-center of the profile. The ADC distribution for the x-coordinate shows a saturating Landau distribution, consistent with expectations at high gain, while the y-coordinate follows the known response behavior.

During the first HV scan of the DUT, the current was recorded simultaneously, enabling

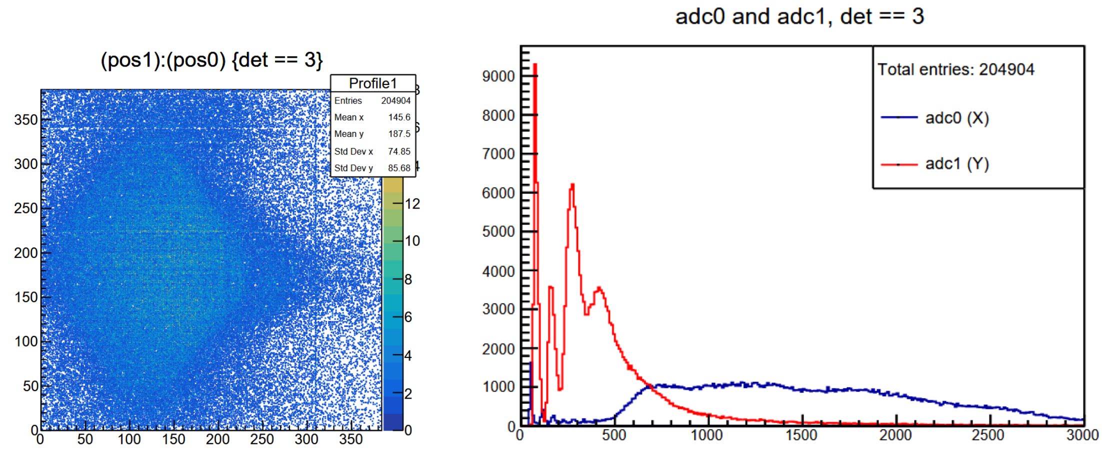

Figure 16: Left: Beam profile in MM3 of the SPS muon beam with the tracker operating at a gain of $\approx 8 \times 10^4$. Right: Corresponding ADC distribution for the x- and y-coordinates. The high detector gain leads to ADC saturation. Approximately 2×10^5 clusters were reconstructed in two extractions, in agreement with the beam monitoring scintillator count of $\approx 2.1 \times 10^5$ events.

determination of the gain curve. The results are shown in Fig. 17. The anode voltage was varied from 390 V to 500 V, with the drift voltage fixed at 200 V. The gain exhibits the expected exponential behavior, with good fit quality. Notably, no photon feedback is observed at the high-voltage end of the scan, unlike the MM3 scan shown in Fig. 8. This difference may arise from detector-to-detector variations or the quenching effect of isobutane. A dedicated gain scan of MM3 with $Ar/CO_2/iC4H10 = 93/5/2$ or $Ar/CO_2 = 93/7$ could help clarify this behavior.

Cleaning

Cleaning of thermally bonded Micromegas requires a careful multistep procedure to ensure both the mesh and the resistive layer are free of dust and contaminants while preserving the detector's integrity. First, the chamber is flushed with isopropanol to dissolve surface impurities and loosen particles. The detector is then opened, and a sticky roller is gently applied to the mesh and also in contact with the resistive layer, effectively removing dust and residual debris without mechanical damage. A second isopropanol rinse follows, during which a noticeable black coloration may be observed in the runoff, indicating the removal of fine carbon-based or resistive material residues. Finally, the detector is baked at 50 °C, well below the melting point of the thermal bonding film ($\approx$ 85 °C), while being continuously flushed with nitrogen to prevent humidity absorption. During this baking step, high voltage is applied and gradually increased, with the voltage held stable each time until the leakage current drops below 1 nA. This procedure is repeated until the operating voltage reaches approximately

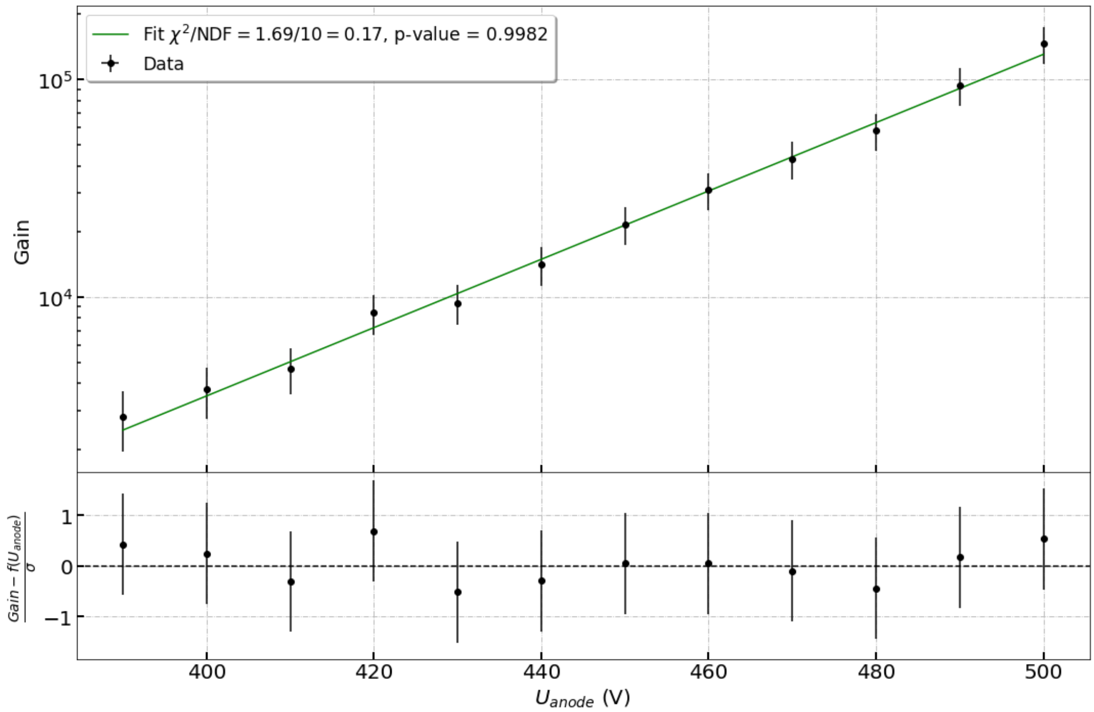

Figure 17: DUT HV scan during the test beam. Detailed characterization of the DUT is given in [14].

700 V, at which point the detector is kept stable at this voltage for about half a day to ensure long-term electrical stability before use.

3.3 Corryvreckan tracking

Corryvreckan is a modular software framework for reconstruction and analysis of pixel detector data, such as silicon pixel detectors [6]. It provides a flexible environment to process raw signals, perform clustering, reconstruct particle tracks, and evaluate detector performance metrics, including spatial resolution, efficiency, noise, and alignment. The software is widely used in test beam campaigns and laboratory studies, offering standardized algorithms and visualization tools for direct comparison between different detector technologies.

In Corryvreckan, a single event corresponds to a timestamped occurrence in which one or multiple particles traverse the detector. Raw signals from individual pixels are digitized and calibrated, then grouped into clusters representing localized charge deposition. Using clusters from multiple layers, tracks are reconstructed by associating clusters across detectors, taking geometry and alignment into account. This modular approach enables studies of cluster sizes, track residuals, fake rates, and overall efficiency [6].

Before reconstruction, the steering and geometry configuration must be defined. Plain-text configuration files control the module sequence and parameters, while a separate geometry file specifies translations and rotations of each detector plane relative to a global coordinate system. Rotations describe tilts of each plane around the coordinate axes and are initially applied to reduce systematic biases. For the thermal-bonded Micromegas trackers, x-strips were found to provide better signal quality than y-strips, so all tracker planes were rotated to align the x-coordinates within the same plane. Determining the initial rotation angles was challenging, so a small-scale model of the telescope was constructed in the control room to visualize orientations. Translations must also be defined: x- and y-offsets are refined during prealignment and alignment, but the z-coordinate along the beam must be measured independently prior to reconstruction. Once geometry is set, Corryvreckan can perform event building, clustering, and hierarchical alignment for both trackers and the DUT.

The first approach utilizes pre-clustered data from the VMM3a/SRS software "vmmsdat" [12]. In this method, Corryvreckan is employed for tracking but not for clustering. The input consists of a ROOT tree containing cluster-level information, including the cluster position, charge, size, and timestamp, with pixels of size equal to the strip pitch (400 µm × 400 µm). Some pre-processing is required before reconstruction: a trigger must be defined, either using an external trigger (like a scintillator) or designating one detector as the trigger, which must be copied under a separate detector ID. Additionally, the coordinate system's origin of the tracker should be set to the center of the reference detector. The [EventLoaderMPGD] module then converts the pre-clustered data into Corryvreckan cluster objects and forwards them to the subsequent analysis chain, which includes prealignment and alignment of the detectors. During event building, the module uses the trigger timestamp as a reference, grouping all clusters within a configurable time window into a Corryvreckan event. These clusters are placed on the Corryvreckan clipboard, along with minimal pixel representations for compatibility with downstream modules. Event-level and detector-level histograms are filled to record cluster counts and monitor detector activity throughout the run.

The second approach bypasses pre-clustering and works directly with the raw hits from the VMM3a strip readout using a new custom module [EventLoaderVm3a] [2]. To accommodate the strip geometry, each 2D detector is redefined as two independent planes: an X-plane and a Y-plane. For example, the X-plane is represented as 256 columns and a single row, while the Y-plane has one column and 256 rows. The pixel pitch is adjusted to reproduce the experimental strip geometry, with one dimension set to the full detector length and the other corresponding to the strip width. Before providing the data to Corryvreckan, the hits must be sorted by time rather than by detector.

Event construction is then performed using the [Metronome module], converting the raw strip hits into pixel objects, followed by clustering using Corryvreckan's standard [Clustering4D] module.

After event construction and clustering, a hierarchical alignment procedure is performed to ensure accurate track reconstruction. First, the trackers undergo a prealignment, in which a coarse correction is applied to account for large offsets or rotations between the detector planes. This step typically uses residual distributions from initial tracks to estimate approximate translations and rotations, providing a starting point for finer corrections. Following prealignment, a full tracker alignment is carried out, refining the positions and orientations of each tracker plane using iterative minimization algorithms that reduce the residuals between measured cluster positions and the predicted track positions.

Once the trackers are well aligned, the DUT prealignment is performed by applying a coarse correction based on the preliminary track projections onto the DUT plane. This ensures that the DUT is roughly positioned within the expected tracking region. Finally, a precise DUT alignment is executed, using the fully aligned tracker information to iteratively adjust the DUT position and rotation.

3.4 Corryvreckan DUT analysis

Using the Corryvreckan framework for track reconstruction, the tracking efficiency and the rate of fake clusters in the DUT were studied. The data in this subsection were taken with an increased gain on the trackers and with MM5 replaced by MM4. The DUT was operated at an anode voltage of 490 V. The fake pixel event map and cluster charge distribution are shown in Fig. 18. Fake clusters are defined as clusters in the DUT that cannot be associated with any reconstructed track in Corryvreckan. The 2D event map reveals a faint beam profile, which likely reflects the limited tracking efficiency. The corresponding charge distribution, that is automatically generated by Corryvreckan, exhibits a multi-peak structure at low ADC values, that could be associated with noise counts. The landau distribution from the "real" beam events, that is visible in the 2D event map, could be visible with higher charge histogram ranges.

For clusters in the DUT that are successfully associated with a reconstructed track, the residual distribution and the efficiency map were evaluated, as shown in Fig. 19. The standard deviation of the 2D residual distribution provides an upper limit on the intrinsic spatial resolution of the DUT, since it also includes contributions from the tracker resolution. The residuals form an elliptic distribution centered at the origin, with most entries contained within ±400 µm, corresponding to the strip pitch, which indicates good alignment between the DUT and the trackers. The 2D efficiency map

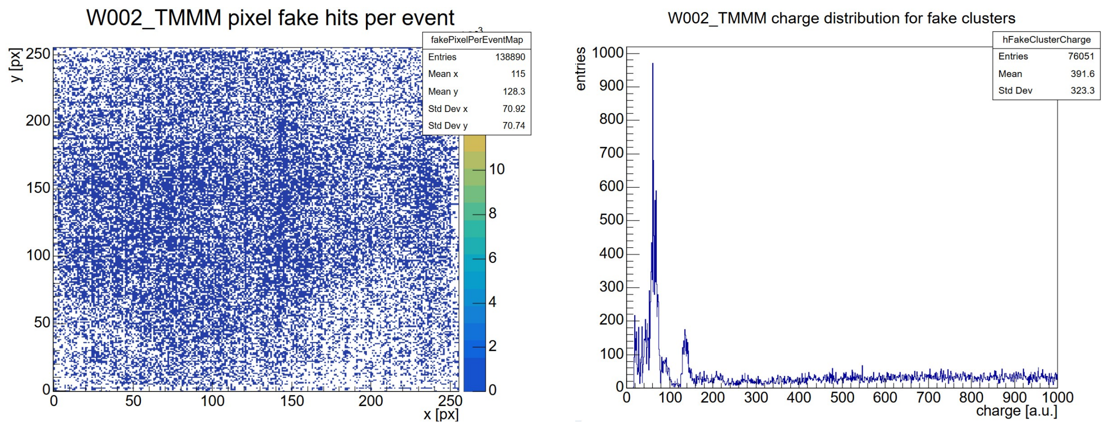

Figure 18: Fake clusters in the DUT. Left: 2D event map of fake clusters, showing a faint beam profile consistent with incomplete tracking efficiency. Right: cluster charge distribution of fake clusters, exhibiting a multi-peak structure at low ADC values, that could be associated with noise counts. The histogram from Corryvreckan has an upper limit of 1024. The landau distribution could be visible with higher charge histogram ranges.

shows a global efficiency of 60–70% across the active detector area, excluding edge regions. Empty tiles are present due to limited statistics and could be reduced with additional data.

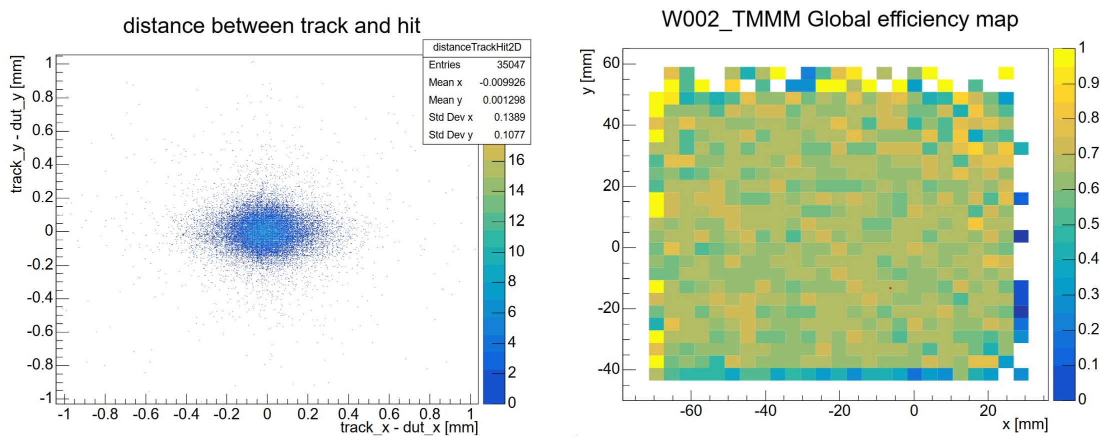

Figure 19: Results for clusters in the DUT associated with reconstructed tracks. Left: 2D residual distribution between reconstructed tracks and associated clusters, with most entries contained within ±400 µm (strip pitch), indicating good alignment between DUT and trackers. Right: 2D efficiency map of the DUT, showing efficiencies between 60–70% across the active area, excluding edge effects.

One can also determine the total detector efficiency as a function of the anode voltage. In gaseous detectors, the efficiency is expected to increase with the applied voltage until all primary ionization electrons are collected and multiplied with sufficiently high gain. At this point, a plateau is reached, as further increases in voltage no longer improve the charge collection. This behavior is confirmed in Fig. 20, where the efficiency rises with increasing anode voltage and saturates at approximately 67% around 460 V. A further increase in the voltage, however, leads to a decrease in efficiency, a behavior that is currently under investigation.

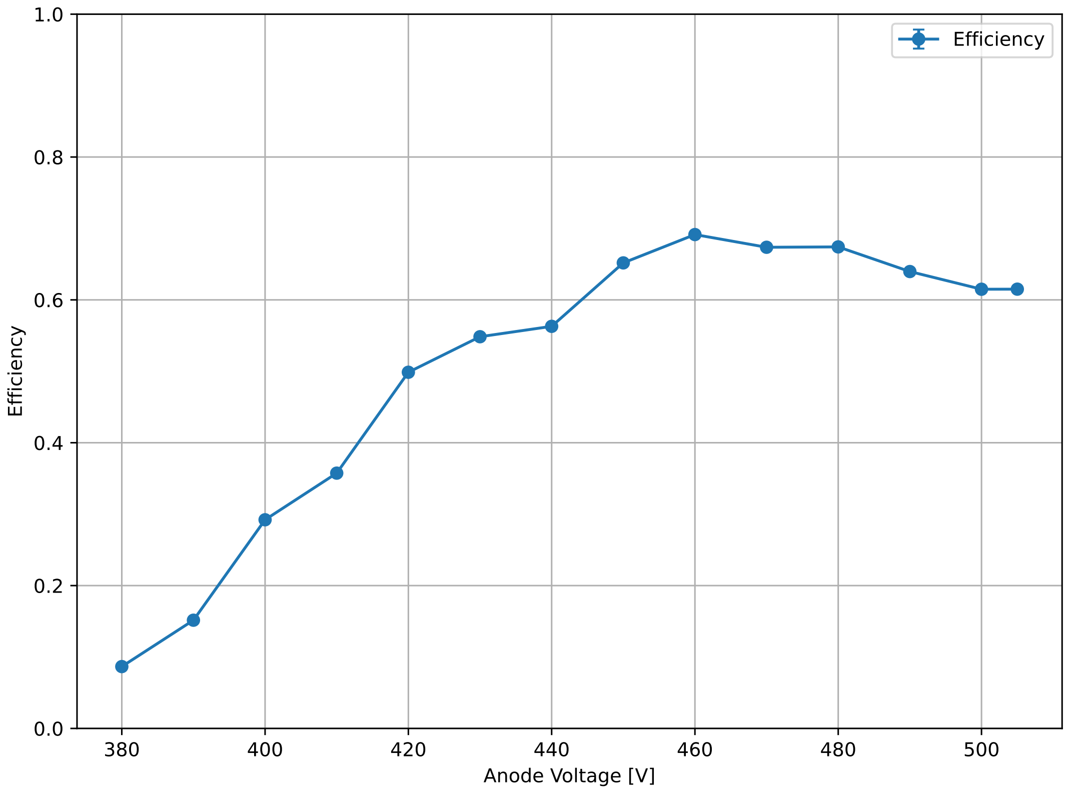

Figure 20: Total detector efficiency of the DUT as a function of the applied anode voltage. The efficiency increases with voltage and reaches a plateau of about 67% around 460 V. At higher voltages, a decrease in efficiency is observed, which is currently under investigation.

The spatial resolution procedure is described in [10]. A double gaussian is fitted to the residual distributions, as shown in Eq. 2. This double gaussian encapsulates the core and tail of the distribution. The resulting tracker resolutions are presented in Fig. 21. The evaluation was performed by including the DUT in the track reconstruction, thereby providing more than two trackers for track finding. This method, however, slightly favors the DUT position. The track resolution is found to be approximately 100 µm in the x-direction and 115 µm in the y-direction. These values are consistent with expectations, as the track resolution is anticipated to be better than the detector pitch divided by $\sqrt{12}$. For an unbiased determination, each tracker must be alternately included and excluded from the track finding. Since the telescope consisted of only three trackers, excluding one left only two points for track fitting. In these cases, the

DUT had to be included as an additional tracking point, which affects the resolution estimate. Future studies could improve the procedure by employing additional trackers, thereby avoiding the need to include the DUT in the reconstruction when one tracker is excluded.

$$G(x) = N\left[a \exp\left(-\frac{(x-\mu)^2}{2\sigma_c^2}\right) + (1-a)\exp\left(-\frac{(x-\mu)^2}{2\sigma_t^2}\right)\right] \tag{2}$$

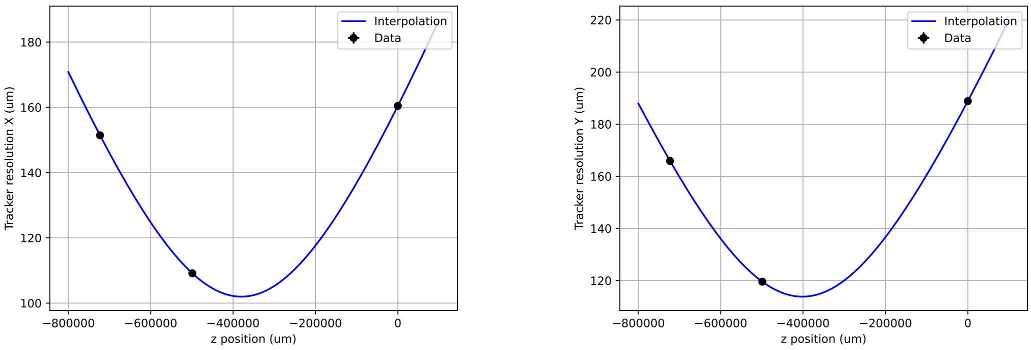

Figure 21: Spatial dependence of the track resolution in the thermal-bonded Micromegas telescope. The spatial resolution was evaluated including the DUT in the track reconstruction, providing more than two trackers for track finding. This procedure introduces a slight bias towards the DUT position. The results indicate a track resolution of approximately 100 µm in the x-direction and 115 µm in the y-direction. These values are consistent with expectations, as the track resolution is anticipated to be better than the detector pitch divided by $\sqrt{12}$. Using more than three trackers in the telescope could mitigate the bias introduced by including the DUT in the reconstruction.

In addition to the tracker resolution, the spatial resolution of the DUT can be evaluated by considering the convoluted residual distribution, which accounts for both the DUT and tracker uncertainties. This is achieved by fitting double Gaussians to the residual distributions, as shown in Fig. 22, where the 2D residual histogram from Fig. 19 has been projected onto the x- and y-axes. In both projections, the core Gaussian dominates the fit, contributing more significantly to the calculated standard deviation than the tail Gaussian. This indicates that most events are tightly clustered around the reconstructed track position, while a smaller fraction of events with larger deviations is described by the tail component.

Table 1 summarizes the spatial resolution results in both x and y directions. The tracker resolution represents the intrinsic resolution of the telescope trackers, determined from the residuals between the reconstructed tracks and the tracker hits. The convoluted DUT resolution includes contributions from both the DUT and the trackers, as obtained

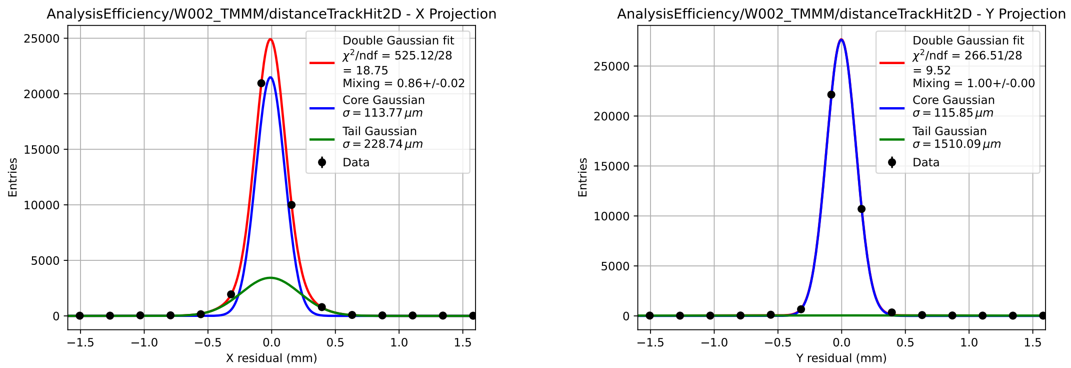

Figure 22: Double Gaussian fits to the projections of the 2D residual histogram from Fig. 19. The x-residual fit is shown on the left and the y-residual fit on the right. In both cases, the core Gaussian dominates the fit, contributing more to the standard deviation than the tail Gaussian.

from the residuals between the DUT clusters and the reconstructed tracks. Finally, the intrinsic DUT resolution is extracted by deconvoluting the tracker contribution from the convoluted resolution, providing an estimate of the DUT's own spatial performance. As previously mentioned, the DUT is rotated by $+90^\circ$ relative to the telescope axes; therefore, the x and y resolutions in the global Corryvreckan coordinates correspond to the y and x spatial resolutions in the detector coordinate system, respectively. The results indicate that the DUT achieves a resolution of approximately 86 μm in x and 57 μm in y, demonstrating the good intrinsic performance of the detector.

Table 1: Summary of spatial resolutions in X and Y. The tracker resolution refers to the intrinsic resolution of the telescope trackers, the convoluted DUT resolution includes contributions from both DUT and trackers, and the DUT resolution is the deconvoluted intrinsic resolution of the DUT.

	X (DUT Y)	Y (DUT X)
Tracker resolution	104.5 μm ± 0.7 μm	118.9 μm ± 0.9 μm
Convoluted DUT resolution	136 μm ± 4 μm	132.0 μm ± 2.1 μm
DUT resolution	86 μm ± 6 μm	57 μm ± 5 μm

4 Conclusion

The goal of this work was the commissioning of a new beam telescope based on thermal bonded Micromegas detectors within the framework of the DRD1 collaboration. Compared to conventional bulk Micromegas, the thermal bonding technique offers simplified fabrication and improved accessibility, while maintaining detector performance. The telescope extends the available infrastructure at the SPS test beam facility and complements the existing GEM-based system with larger active areas and VMM3a/SRS readout electronics.

The project began with detailed laboratory studies, where the Micromegas detectors and the VMM3a/SRS readout chain were thoroughly characterized. Gain scans and drift scans quantified the detector response, and the effect of collimation on the measured energy resolution was observed. While the detectors were generally stable under controlled conditions, some required cleaning to restore proper operation. Additionally, measurements revealed limitations in the y-coordinate response due to the strip geometry, as the strips are embedded approximately $\mathcal{O}(100\,\mu\text{m})$ deep within the insulating layer and not $\mathcal{O}(10\,\mu\text{m})$, reducing the induced signal in that direction. Overall, the laboratory studies demonstrated that the full readout electronics could be operated reliably.

In the second phase, the telescope was deployed at the SPS test beam line, where its performance under real beam conditions was evaluated. Multiple data-taking runs were conducted, including systematic high-voltage scans. Operational challenges such as detector discharges were successfully mitigated by cleaning and flushing procedures, restoring stable performance. Beam profiles were reconstructed, and an additional gain scan of the DUT was carried out during the campaign. These results demonstrated that the system was capable of continuous operation in a high-rate beam environment.

For tracking analysis, Corryvreckan was employed, starting from the pre-clustered vmm-sdat input approach. Detector geometry and rotations were implemented, allowing both alignment and pre-alignment procedures to be carried out successfully. First results with Corryvreckan were shown: a good residual distribution was obtained, and the spatial resolution of the telescope and the DUT was determined. Although efficiency studies are still ongoing, these initial results validate the use of Corryvreckan for this novel Micromegas-based telescope.

In summary, the commissioning goals were achieved. The laboratory setup confirmed the correct functioning of the electronics, while also revealing limitations in the y-coordinate response due to the strip geometry, as the strips are embedded $\mathcal{O}(100\,\mu\text{m})$ deep within the insulating layer. The test beam campaign demonstrated stable detector operation, provided tracking data, and delivered the first spatial resolution results of the DUT. Together, these results establish a foundation for the future use of the telescope in beam tests, where its large active area, modern readout, and integration with Corryvreckan will provide support for detector development in the DRD1 collaboration.

The preliminary results obtained with the $15 \times 15\,\text{cm}^2$ Micromegas detectors are promising and indicate that further studies with this detector size would be worthwhile. Future efforts could focus on extending the test beam measurements to collect more statistics. Additionally, more time could be dedicated to refining the Corryvreckan reconstruction, aiming to improve tracking efficiency and residuals. This includes implementing the approach where raw hit data are directly clustered within Corryvreckan, rather than relying on pre-clustered input. Finally, upgrading the telescope with Micromegas detectors featuring optimized y-strips would help overcome the current limitations related to the strip geometry.

5 Acknowledgments

I would like to take this opportunity to thank several people who contributed to my work. First and foremost, I am deeply grateful to Karl Jonathan Floethner and Dr. Eraldo Oliveri for giving me the opportunity to participate in the CERN Summer Student Programme in the GDD laboratory with the DRD1 collaboration. I would also like to thank Dr. Lucian Scharenberg for his dedicated efforts in teaching me the VMM3a/SRS readout system, including hardware, firmware, and software. My sincere thanks go to Dr. David Marques for patiently working with me to resolve every the vmm-sdat issues that we encountered together. I am also grateful to Anna Milieva, whose support was crucial for the initial progress in Corryvreckan tracking. Finally, I would like to thank all members of the GDD laboratory and the DRD1 collaboration for their continuous help, guidance, and for making my time at CERN both productive and enjoyable.

Bibliography

[1] DRD1 Working Group 5. *VMM3a/SRS Documentation.* (accessed 30-August-2025). URL: https://vmm-srs.docs.cern.ch/.

[2] Antti Lumppio. *Corryvreckan analysis tool for MPGDs: Different possibilities of raw data integration.* (accessed 30-August-2025). URL: https://indico.cern.ch/event/1442324/contributions/6262059/attachments/2986117/5259291/2024_DRD1_WG7_presentation_corry_ALumppio.pdf.

[3] David Attié et al. "Current Status and Future Developments of Micromegas Detectors for Physics and Applications". In: *Applied Sciences* 11.12 (2021). ISSN: 2076-3417. DOI: 10.3390/app11125362. URL: https://www.mdpi.com/2076-3417/11/12/5362.

[4] Maximilien Chefdeville. *Development of micromegas-like gaseous detectors using a pixel readout chip as collecting anode.* May 2009.

[5] PICOSEC collaboration. *PICOSEC Micromegas.* (accessed 30-August-2025). URL: https://picosec-mm.web.cern.ch/.

[6] D. Dannheim et al. "Corryvreckan: a modular 4D track reconstruction and analysis software for test beam data". In: *Journal of Instrumentation* 16.03 (Mar. 2021), P03008. ISSN: 1748-0221. DOI: 10.1088/1748-0221/16/03/p03008. URL: http://dx.doi.org/10.1088/1748-0221/16/03/P03008.

[7] Jianxin Feng et al. "A thermal bonding method for manufacturing Micromegas detectors". In: *Nuclear Instruments and Methods in Physics Research Section A: Accelerators, Spectrometers, Detectors and Associated Equipment* 989 (2021), p. 164958. ISSN: 0168-9002. DOI: https://doi.org/10.1016/j.nima.2020.164958. URL: https://www.sciencedirect.com/science/article/pii/S0168900220313553.

[8] I. Giomataris et al. "Micromegas in a bulk". In: *Nuclear Instruments and Methods in Physics Research Section A: Accelerators, Spectrometers, Detectors and Associated Equipment* 560.2 (2006), pp. 405–408. ISSN: 0168-9002. DOI: https://doi.org/10.1016/j.nima.2005.12.222. URL: https://www.sciencedirect.com/science/article/pii/S0168900205026501.

[9] Y. Giomataris et al. “MICROMEGAS: a high-granularity position-sensitive gaseous detector for high particle-flux environments”. In: *Nuclear Instruments and Methods in Physics Research Section A: Accelerators, Spectrometers, Detectors and Associated Equipment* 376.1 (1996), pp. 29–35. ISSN: 0168-9002. DOI: https://doi.org/10.1016/0168-9002(96)00175-1. URL: https://www.sciencedirect.com/science/article/pii/0168900296001751.

[10] Lucian Simon Scharenberg. “Next-Generation Electronics for the Read-Out of Micro-Pattern Gaseous Detectors”. PhD thesis. Rheinische Friedrich-Wilhelms-Universität Bonn, Apr. 2023. URL: https://hdl.handle.net/20.500.11811/10776.

[11] Marcin Byszewski. *Development of resistive-strip micromegas for the ATLAS upgrade.* (accessed 30-August-2025). URL: https://agenda.infn.it/event/3950/contributions/49540/attachments/34898/41194/byszewski_micromegas.pdf.pdf.

[12] Maryna Borysova. *Corryvreckan analysis tool for MPGDs: Track reconstruction with VMM3a/SRS data.* (accessed 30-August-2025). URL: https://indico.cern.ch/event/1442324/contributions/6262058/attachments/2986076/5259208/corry_presentation_mb.pdf.

[13] Michael Vogt. *Trigger counter for synchronization of readouts.* (accessed 30-August-2025). URL: https://indico.cern.ch/event/1543925/contributions/6567175/attachments/3087819/5468058/event-counter-drd1-meeting.pdf.

[14] L. Scharenberg et al. “Characterisation of resistive MPGDs with 2D readout”. In: *Journal of Instrumentation* 19.05 (May 2024), P05053. DOI: 10.1088/1748-0221/19/05/P05053. URL: https://dx.doi.org/10.1088/1748-0221/19/05/P05053.

[15] L. Scharenberg et al. “Development of a high-rate scalable readout system for gaseous detectors”. In: *Journal of Instrumentation* 17.12 (Dec. 2022), p. C12014. DOI: 10.1088/1748-0221/17/12/C12014. URL: https://dx.doi.org/10.1088/1748-0221/17/12/C12014.

[16] Joerg Wotschack. “The development of large-area Micromegas detectors for the ATLAS upgrade”. In: *Mod. Phys. Lett. A* 28 (2013), p. 1340020. DOI: 10.1142/S0217732313400208. URL: https://cds.cern.ch/record/1709400.